

Article

The Effects of Induction Plasma Spheroidization on the Properties of Yttrium-Stabilized Zirconia Powders and the Performance of Corresponding Thermal Barrier Coatings for Gas Turbine Engine Applications

Haoran Peng^{1,2,3}, Yueguang Yu^{1,4,*}, Jianxin Dong¹, Tianjie Shi², Kang Yuan^{2,3}, Zheng Yan^{2,3}  and Botian Bai²

- ¹ School of Materials Science and Engineering, University of Science and Technology Beijing, Beijing 100083, China; weixuan2007@163.com (H.P.); jxdong@ustb.edu.cn (J.D.)
- ² BGRIMM Technology Group, Beijing 100160, China; shi981204@163.com (T.S.); yuankang@bgrimm.com (K.Y.); z_yan0926@163.com (Z.Y.); ibaibotian@163.com (B.B.)
- ³ BGRIMM Advanced Materials Science & Technology Co., Ltd., Beijing 102206, China
- ⁴ China Iron & Steel Research Institute Group, Beijing 100081, China
- * Correspondence: yuygbgrimm@163.com

Abstract: To modify the structure of thermal barrier coatings and improve their high-temperature resistance, induction plasma spheroidization (IPS) technology was applied to regulate the structure of YSZ powders in this study. The surface morphology, particle size distribution, phase composition, and internal microstructure of the conventional agglomerated and spheroidized powders were characterized using scanning electron microscopy and focused ion beam analysis methods. The results showed that the microstructure of the powders presented uneven evolution in the induction plasma stream. Due to the existence of the temperature gradient along the radial direction of the powders, the IPS powders consisted of outer dense shells and internal porous cores. The mechanical property of such shell–core structure was analyzed by using the finite elemental simulation method. In addition, coatings were prepared using the IPS powders and the agglomerated powders. The IPS coating showed improved water-cooling thermal cycling resistance compared to the conventional coating.

Keywords: induction plasma spheroidization; TBC; shell–core structure; coating performance improvement



Citation: Peng, H.; Yu, Y.; Dong, J.; Shi, T.; Yuan, K.; Yan, Z.; Bai, B. The Effects of Induction Plasma Spheroidization on the Properties of Yttrium-Stabilized Zirconia Powders and the Performance of Corresponding Thermal Barrier Coatings for Gas Turbine Engine Applications. *Coatings* **2024**, *14*, 627. <https://doi.org/10.3390/coatings14050627>

Academic Editor: Narottam P. Bansal

Received: 28 March 2024

Revised: 18 April 2024

Accepted: 22 April 2024

Published: 16 May 2024



Copyright: © 2024 by the authors. Licensee MDPI, Basel, Switzerland. This article is an open access article distributed under the terms and conditions of the Creative Commons Attribution (CC BY) license (<https://creativecommons.org/licenses/by/4.0/>).

1. Introduction

Gas turbines are a type of power machinery that utilize the energy of high-temperature gases to drive the rotor at high speeds and are extensively used in the fields of aviation and aerospace [1]. The goal of researchers is to further improve the thrust-to-weight ratio and thermal efficiency of the gas turbines by increasing the operating temperature of the combustion chamber. That brings a significant challenge to the high-temperature performance of the gas turbine components [2]. Over the past few decades, the performance of gas turbines has been greatly enhanced due to the successful application of thermal barrier coatings (TBCs) [3]. Yttria-stabilized zirconia (YSZ) has become the most successful material, owing to its excellent comprehensive high-temperature properties [4–7]. However, the conventional preparation method of YSZ powder usually leads to some problems for the TBCs such as insufficient high-temperature capability, low bonding strength, and phase transformation [8–11]. Consequently, there is a need to optimize the YSZ powder to accommodate operations at elevated temperatures.

Induction plasma spheroidization (IPS) is an innovative technology for powder shaping [12,13]. The IPS process utilizes the hot plasma to rapidly heat and melt powders, which can remove some microdefects and impurities from the powders [14,15]. Researchers

have developed advanced models to study the IPS process, which aids in a better understanding of the powder spheroidization behavior [16,17]. During the heating process, the molten metal particles can transfer to spherical droplets under the influence of surface tension. The droplets then rapidly solidify into spherical powders with enhanced properties [18–20]. Through the use of the IPS technology, the structure of ceramic powders can also be controlled to achieve specific structures and properties [21–23]. Current research in this area is ongoing, but there is a scarcity of studies on the effect of the IPS treatment on the microstructure and properties of YSZ powders used in thermal barrier coatings.

This paper investigated the differences between agglomerated YSZ powders and IPS powders in terms of powder morphology, internal structure, and phase composition. By applying finite elemental modeling, it analyzed the trend of particle deformation under compression conditions to understand the transformation behavior from powder structure to coating structure. The current paper also compared the water-quenching thermal shock resistance between the coatings prepared using the two types of powders.

2. Materials and Methods

2.1. Preparation of YSZ Powders

YSZ particles (yttrium oxide ratio: ~7.5 wt.%) with a purity of 99.9% (total content of zirconia and yttrium oxide) and a size of 1–3 μm (BGRIMM Advanced Materials Science & Technology Co., Ltd., Beijing, China) were used as raw materials. The raw particles were mixed with a solution containing deionized water (as the dispersion medium), polyvinyl alcohol (as the binder), and some zirconia balls (as the grinding balls) in the GJ-2000 drum miller (Xianyang Jinhong General Machinery Ltd., Xianyang, China). After a certain period of milling time (the grinding elements are zirconia balls with a diameter of 6 mm), a stable and uniform ceramic slurry was obtained in which the solid content of the ceramic powders was 62.5%. The ball-milled slurry was then sent into a high-speed centrifugal spray dryer (LGZ-8, Wuxi Dongsheng spray drying equipment Co., Ltd., Wuxi, China) to prepare agglomerated powders. In this process, the slurry was transferred from a feeding system to a nozzle to be atomized to produce foggy droplets. The droplets were then heated by hot air (120–300 $^{\circ}\text{C}$) in the drying tower. When the water in the droplets was evaporated, solid agglomerated powders were obtained at the bottom of the tower. The powders were calcined at 1000 $^{\circ}\text{C}$ for 3 h to remove the binder. The agglomeration parameters are shown in Table 1. The agglomerated powders used for the post IPS treatment were sieved to obtain a particle size range from 25 μm to 75 μm .

Table 1. The process parameters of centrifugal spray drying.

Inlet Temperature ($^{\circ}\text{C}$)	Outlet Temperature ($^{\circ}\text{C}$)	Feed Rate (Hz)	Spray Disc Speed (rpm)
300	120	30	40

An induction plasma spheroidizing (IPS) system (TEKNA-80, TEKNA, Quebec City, QC, Canada) was used to spheroidize the agglomerated ceramic powders. The maximum power of the IPS equipment was 80 kW by using Ar and H_2 as the main gas and the auxiliary gas. The IPS parameters used to make the IPS powders are shown in Table 2. To achieve a relatively high density of the powders, three cycles of the IPS treatment were performed.

Table 2. Induction plasma spheroidization process parameters.

Power (kW)	Pressure (psi)	Carrier Gas, Ar (slpm)	Ar Flow (slpm)	H_2 Flow (slpm)	Feeder Rate (g/min)
80	15	95	30	15	40

2.2. Preparation and Testing of Coatings

Two types of coatings, namely, a conventional coating and an IPS coating, were prepared by using the agglomerated YSZ powders and the IPS YSZ powders on a nickel-based superalloy substrate (GH5188, $\Phi 30 \times 5$ mm) with NiCoCrAlY (Amry365-4) bond coatings. The NiCoCrAlY bond coating was made by using the HVOF (High-Velocity Oxy-Fuel) technique in the GTV-MF-P-HVOF-K-ARC-200 system. The YSZ top coating was made by using the APS (Atmospheric Plasma Spray) process in the Metco F6 system. The coatings' thicknesses were ~ 100 μm (bond coat) and ~ 150 μm (top coat), respectively. The spraying parameters are listed in Tables 3 and 4.

Table 3. Spraying parameters of MCrAlY bond coat.

Parameter	Values
Kerosene (L/min)	24
Primary gas, O ₂ (L/min)	900
Carrier gas, Ar (L/min)	3.5
Stand-off distance (mm)	360
Powder feed rate (g/min)	30
Tooling speed (r/min)	100

Table 4. Spraying parameters of YSZ top coat.

Parameter	Values
Power (kW)	46
Primary gas, Ar (L/min)	38
Secondary gas, H ₂ (L/min)	13
Carrier gas, Ar (L/min)	4.5
Stand-off distance (mm)	100
Powder feed rate (g/min)	25
Tooling speed (r/min)	30

The conventional and IPS coating samples were tested by using water quenching-thermal shock cycling. One cycling process included a heating stage at 1100 °C for 5 min in a box furnace and a cooling stage by quenching the samples in pure water to room temperature. The cycling process was repeated until the area peeling ratio of the top coatings exceeded 10%. The macroscopic morphology of samples was recorded every 50 cycles.

The conventional and IPS coating samples were tested by using water quenching-thermal shock cycling. One cycling process included a heating stage at 1100 °C for 5 min in a box furnace and a cooling stage by quenching the samples in pure water to room temperature. The cycling process was repeated until the area peeling ratio of the top coatings exceeded a certain percentage. At the edges of the samples were areas with large structural transformation, it was common for coatings to experience localized and random delamination due to stress concentration during thermal cycling tests. In the thermal shock testing, some very small starting edge delamination (for example less than 5%) could not indicate the coating failure. The commonly used percentage to define the coating failure was 10%~30%. In this study, we chose 10% as the threshold for coating failure. The macroscopic morphology of samples was recorded every 50 cycles.

2.3. Characterization and Simulation

The surface morphology and cross-sectional microstructure of the powders and coatings were analyzed in a scanning electron microscope (SEM, SU5000, Hitachi Ltd., Tokyo, Japan). The phase structure of the powders was determined by X-ray diffraction (XRD, Bruker D8 Advanced, Karlsruhe, Germany) with Cu-K α radiation. Digital data were gathered in a continuous scan mode with a scanning rate of 0.2°/s and 2 θ angle range of 20~80°.

The size of the powders was measured in a laser particle size analyzer (Mastersizer3000, Malvern, UK).

The internal microstructure of the IPS YSZ powder was also analyzed by using a cutting FIB SEM imaging technique in the Zeiss Auriga FIB/SEM hybrid system. A Ga liquid metal ion source with an accelerate voltage of 30 kV and a beam current of 50 Ma was applied. To increase conductivity, a nano-thick layer of gold was deposited on the top of the YSZ powders. The studied powders were put on a metallic copper conductive tape. A series of SEM images could be recorded layer-by-layer as the FIB system cut material from a selected YSZ powder.

Finite elemental modeling (FEM) was performed using the codes ABAQUS to investigate the effect of a dense shell on the stress distributions in the IPS YSZ powders. In the shell, the material was simply assumed to be elastic. The material constants employed in the FEM analysis were Young's modulus of 75 GPa and Poisson's ratio of 0.25. A force of 0.1 N was exerted onto the top of the particles with a contacting area of radius 5 μm . Two different powder structures were simulated for comparison. One was fully dense and the other had a shell-core structure with a shell thickness of 5 μm . In the shell-core structure, the porous core was treated as no stress being sustained. The particle radius was set as 25 μm .

3. Results and Discussion

3.1. Characterization of the Agglomerated YSZ Powders

The surface morphology and cross-sectional microstructure of the agglomerated YSZ powders are shown in Figure 1. The powder was nearly spherical, with a particle size of approximately 20–80 μm (Figure 1a). Figure 1b shows the magnified surface structure of a single powder, which was composed of many nanoparticles with a size of ~50 nm and numerous pores among the nanoparticles. The cross-sectional SEM image (Figure 1c) shows that the internal structure of the powders was also composed of small particles and pores. A single powder was randomly selected for EDS element distribution analysis, as shown in Figure 1d. It was found that the distribution of Zr and Y elements was relatively uniform in the powder.

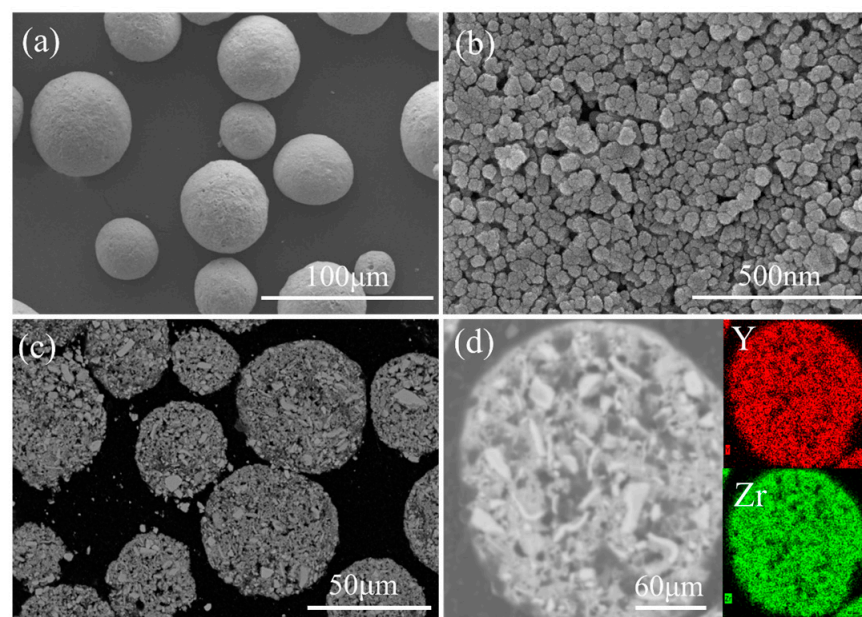


Figure 1. The microstructure of agglomerated YSZ powders: (a) the surface morphology with low magnification, (b) a magnified surface SEM image of a single powder, (c) the cross-sectional morphology with low magnification, and (d) EDS mapping results of the cross-section of a single powder.

3.2. Characterization of the IPS YSZ Powders

Figure 2 shows the morphology of the IPS powders. The powders had excellent sphericity and presented a smooth and dense surface. The magnified morphology further showed that both the nanoparticles and pores were eliminated after the IPS treatment. Instead, a dense surface was formed with obvious growth of grain size. Based on the results in Figure 3a, compared to the particle size curve of the agglomerated powders, the IPS powders' curve showed a left shift and became narrower, indicating that the IPS powders had a certain degree of shrinkage and were more uniform in particle size, which was the result of pore elimination. The XRD measurement (Figure 3b) shows that there was no significant phase changes in the powders after the IPS treatment. The $t\text{-ZrO}_2$ was still the dominant phase. A small amount of the $m\text{-ZrO}_2$ phase was also detected at the peak around 28° , which is common and acceptable for the YSZ powders.

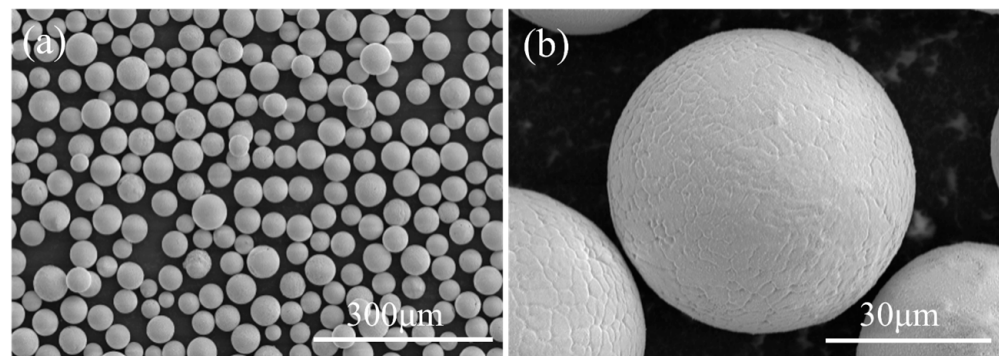


Figure 2. The surface morphology of the IPS-treated YSZ powders: (a) SEM with low magnification and (b) a magnified image of a single powder.

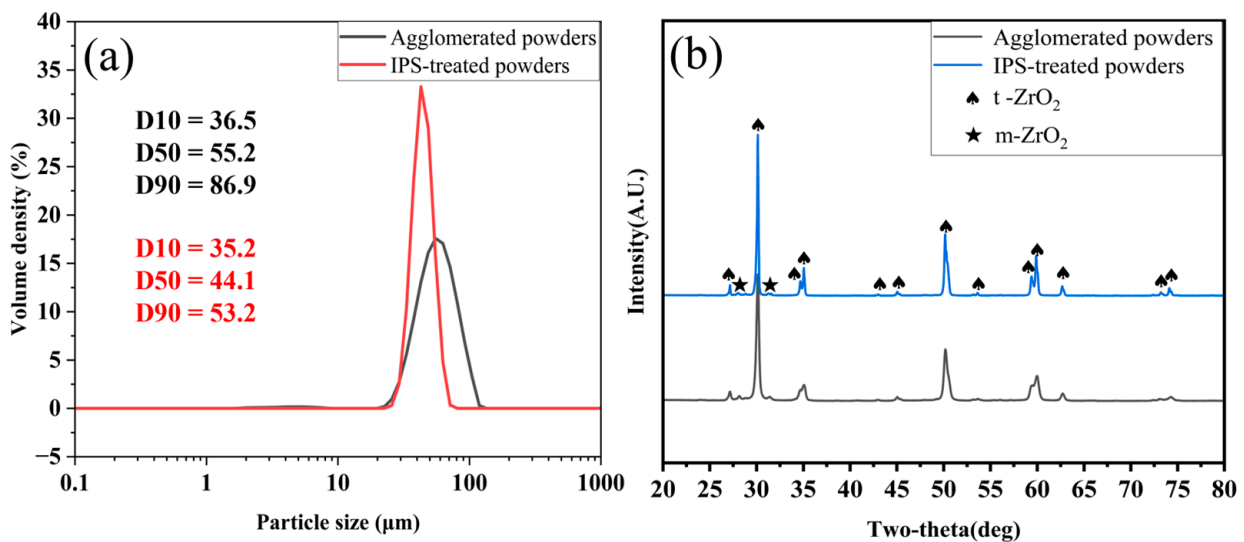


Figure 3. (a) Particle size measurement; (b) phase structure measurement.

Figure 4 gives an illustration of the melting process of an agglomerated YSZ powder during the IPS treatment. When passing through the hot plasma stream, the injected powder instantly absorbed heat at the surface. The small particles at the surface were first molten and then became a dense shell in the following cooling process. Some pores inside of the powder would be ejected and the internal structure of the powder could become denser as well. As the melting point of YSZ is high and the thermal conductivity is low (the melting point of YSZ is 2720°C and its thermal conductivity value is $1.0\text{--}1.2\text{ W/m}\cdot\text{K}$) [24], the YSZ powder usually cannot be fully densified. As a result, the powder could form a

shell–core structure. By increasing the heating time of the powders, e.g., by repeating the IPS process several times, the powder density can be further improved.

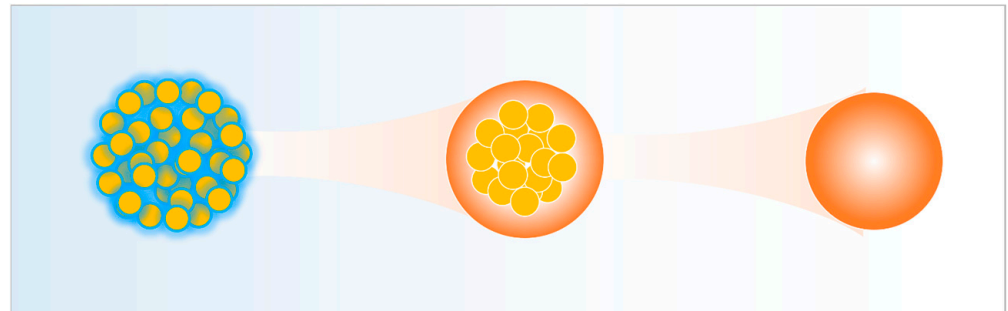


Figure 4. A schematic drawing of the microstructural evolution of the YSZ powder during the IPS treatment.

Figure 5 provides typical internal structures of an IPS YSZ powder. By applying the FIB technique, a series of the cross-sections were imaged. The results show that the powder had a relatively dense spherical morphology. The outer shell part was fully dense, while the internal core had some pores (Figure 6). The energy of the plasma was very high, so the shell layer could be sufficiently densified. As the depth of sectioning increased, some pore defects appeared in localized areas. When the fine particles inside of the powder were sintering and increasing in size, some gaps were inevitably retained to form a porous core. By repeating the IPS process (three cycles), the internal structure of the powder became dense enough. The EDS maps of the internal cross-section of the powder indicate the uniformity of the elemental distribution.

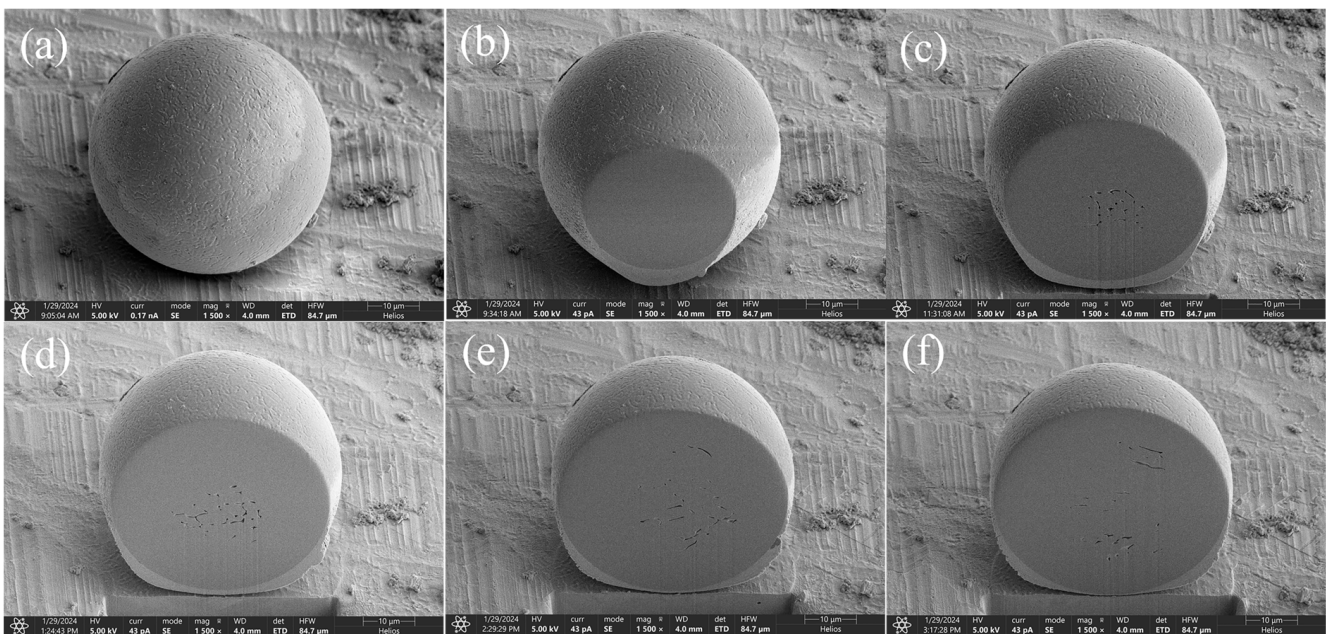


Figure 5. Various cross-sections of a YSZ particle obtained during cutting by the FIB system. (a) original particle. (b) cut once particle. (c) cut twice particle. (d) cut thrice particle. (e) cut four times particle. (f) cut five times particle.

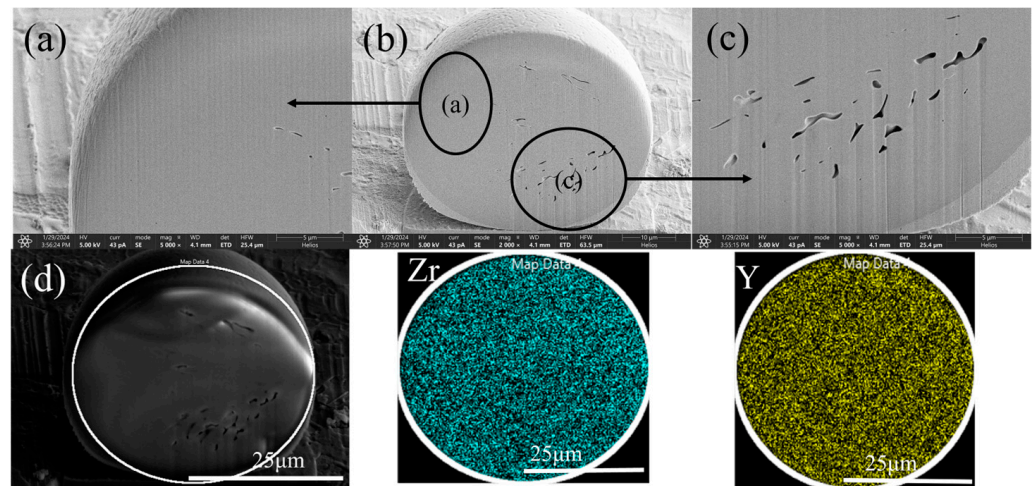


Figure 6. The internal microstructure of the IPS powder and the EDS maps of the internal cross-section. (a) high magnification image of area of particle a. (b) low magnification image of particle. (c) high magnification image of area of particle c. (d) particle element surface scanning area.

Figure 7 shows the contour of maximum principle stress in the two types of particles. The results indicate that the stress distribution was strongly affected by the shell structures. The particle model did not consider the porosity gradient in this study. The porosity gradient throughout the thickness of the particle was simply assumed to be non-stress sustaining in this study. All of the particles sustained the main compressive stresses at the top and bottom of the particles' external surface. The largest tensile stress in the fully dense powder occurred at the outer part of the equatorial plane. For the shell-structured particle, the internal surface of the shell tended to sustain a maximum tensile stress, indicating that the shell would be broken from inside first. Because the powders used for coating preparation had a very dense structure in this study, the IPS powders would be deformed in a similar way to those in the case presented in Figure 7a. The core of the IPS powder under compression was mainly condensed rather than stretched.

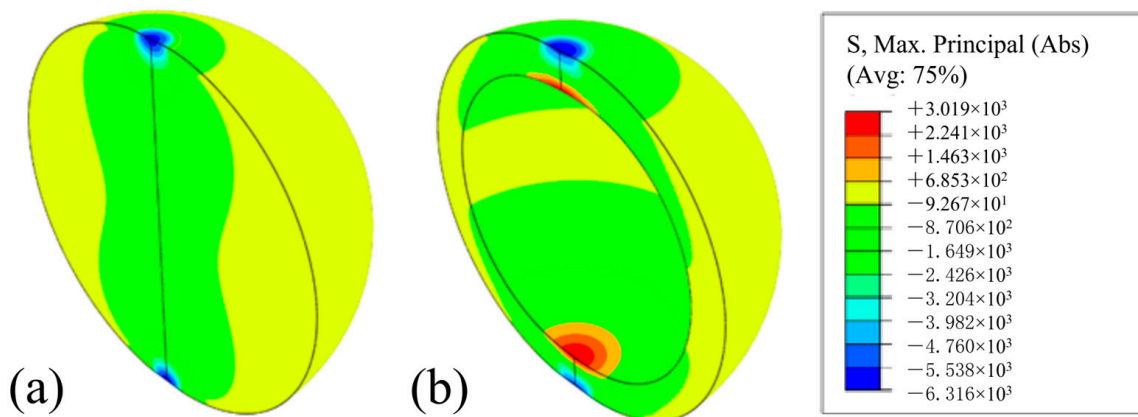


Figure 7. Max. principle stress map for particles (radius 25 μm) with different shell thicknesses: (a) fully dense powder; (b) powder with shell thickness of 5 μm .

3.3. Plasma-Sprayed YSZ Coatings

The polished cross-sectional microstructure of the coatings prepared by using the agglomerated powders and the IPS powders is shown in Figure 8. The conventional YSZ coating had a looser structure with larger pores, while the IPS coating had a denser and more homogeneous structure with smaller pores. The rough matrix of the conventional coating contained some unmelted or partially melted particles. In contrast, the microstructure of the IPS coating was smooth, containing small pores. Due to the denser internal structure of

the IPS powders, the IPS coating showed better stacking deposition among individual flat particles, which would effectively reduce the number of micropores and microcracks in the coatings. The deposition of the powders on the substrate contained two basic behaviors for shells and cores. The outer shells were molten and functioned by bonding with the other splats. The internal cores were under a compression process when the powder impacted on the substrate. According to the FEM results in Figure 7a, the IPS powder under compression would be mainly condensed rather than stretched, so a dense matrix of the coating can form.

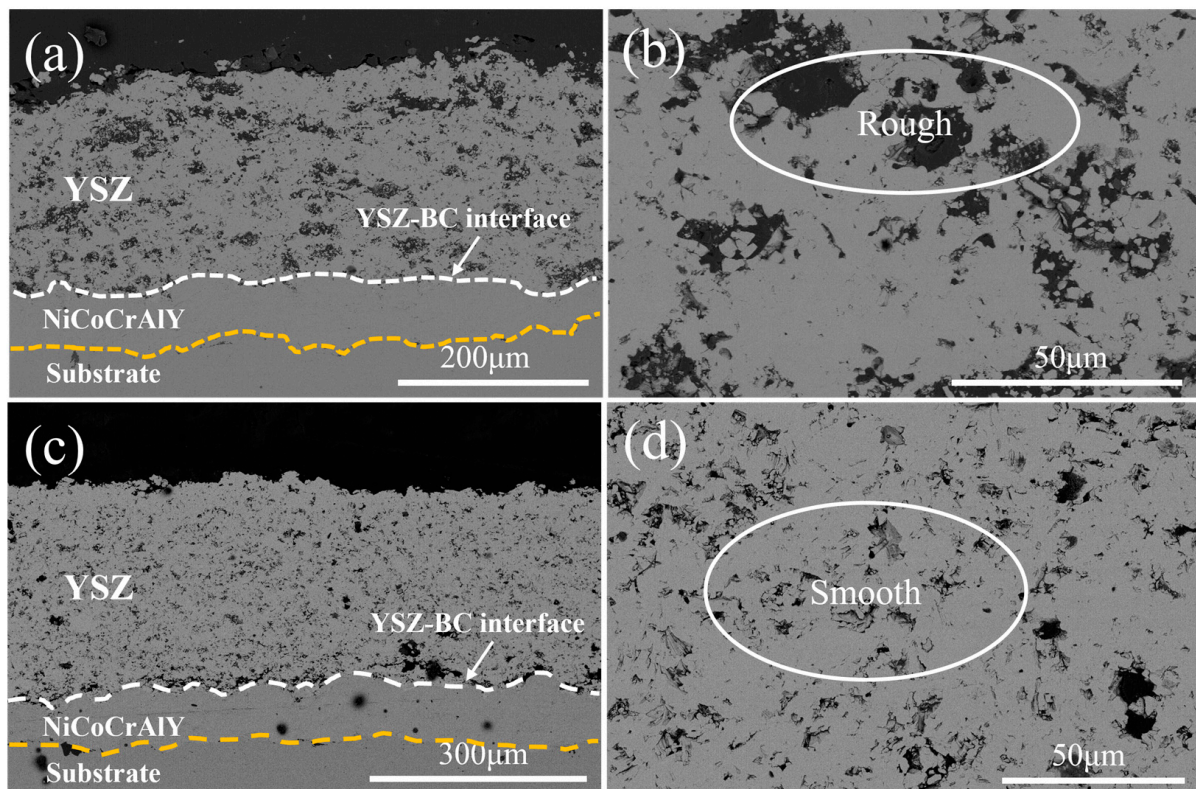


Figure 8. The cross-sectional microstructure of the YSZ coatings: (a) the conventional coating using the agglomerated powders, (b) the morphology with higher magnification of (a), (c) the IPS coating using the IPS powders, and (d) the morphology with higher magnification of (d).

Due to the mismatch in the thermal expansion coefficients between the YSZ top coat and the bond coat, substantial internal stress was generated which can cause cracking and spalling of the top coat. To effectively characterize the impact of the IPS process on the service life of the coating, this study employed a thermal cycling method involving heating and soaking at 1100 °C followed by water-cooling to accelerate the degradation assessment of the coated samples. It was important to note that the edges of the samples were regions with large structural change and were subject to edge effects during water-cooling thermal shock cycling, which can result in random, localized delamination. By using 10% as the criteria of the delamination area percentage, the IPS coating failed after 312 thermal cycles, while the traditional coating failed after 126 cycles according to the result in Figures 9 and 10.

Figure 9 presents the macroscopic morphology of the conventional TBC during water-quenching thermal shock testing. Prior to the thermal shock experiment, the surface of the coating was nearly white. During the thermal shock cycles, the surface of the coating gradually turned yellow and darker, likely due to the oxidation of the bond coat. After 126 cycles, the area of peeling exceeded 10%. Such experimental result agreed well with the literature data when using the similar powder and coating structures [25]. In contrast, the

IPS coating exhibited 10% coating peeling after 312 cycles as shown in Figure 10. Therefore, the IPS coating demonstrated greater sustainability in water-cooled thermal shock testing compared to the conventional coating, effectively extending the service life of the coating under water-cooled thermal shock conditions.

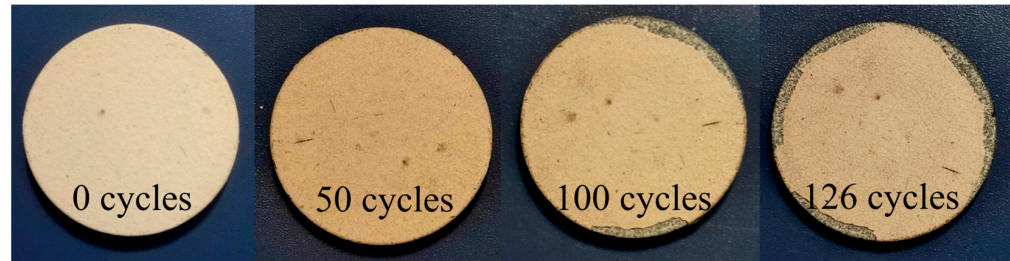


Figure 9. Macroscopic morphology of conventional TBC during water-quenching thermal shock testing.

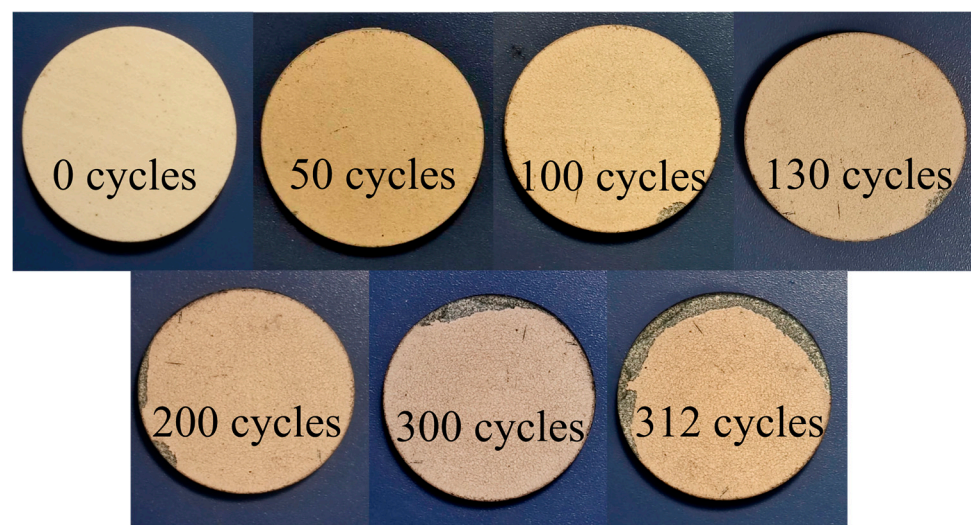


Figure 10. Macroscopic morphology of IPS TBC during water-quenching thermal shock testing.

The interface microstructure of the TBCs after water-quenching thermal shock testing is shown in Figure 11. Both the conventional and IPS coatings showed a similar cracking mechanism. The YSZ top coats spalled along the bond coating surface because of the thermal stresses caused by the expansion mismatch between the YSZ and the metallic bond coat. The IPS coating had a longer cycling life probably because of the coating having a denser and more uniform matrix and less microdefects, which delayed the cracking of the YSZ top coat.

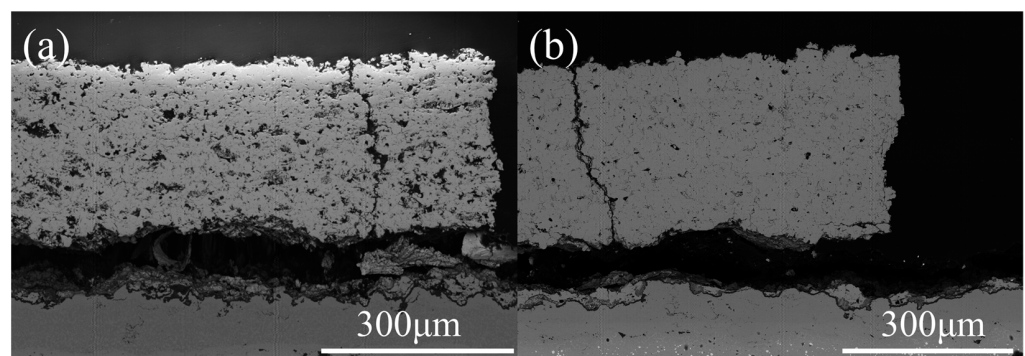


Figure 11. The interface microstructure of the TBCs after water quenching-thermal shock testing: (a) the conventional coating after 126 cycles and (b) the IPS coating after 312 cycles.

4. Conclusions

This study conducted a comprehensive analysis of the effects of the IPS technique on the properties of YSZ powders and the performance of TBCs made from the corresponding YSZ powders.

Regarding the powders, the IPS treatment led to the formation of the desirable fully dense powders with significantly improved chemical homogeneity and stress uniformity. Regarding the coatings, the coatings made by the IPS-treated powders had a denser and more homogeneous microstructure, compared with the ones made from the conventional agglomerated powders. Thermal shock resistances of the above coatings were further compared by water-quenching cycling tests. The IPS coating failed after 312 thermal cycles, while the traditional coating failed after 126 cycles. The cycle life of the IPS coating had been more than twice that of the traditional coating, indicating that the IPS coating had significantly improved thermal cycling resistance, which could be attributed to the IPS-treated feedstock which had excellent properties.

Author Contributions: Conceptualization, H.P. and Y.Y.; methodology, H.P.; validation, H.P., T.S., and K.Y.; formal analysis, H.P. and T.S.; investigation, H.P. and B.B.; data curation, H.P. and T.S.; writing—original draft preparation, H.P.; writing—review and editing, Z.Y. and K.Y.; supervision, Y.Y. and J.D. All authors have read and agreed to the published version of the manuscript.

Funding: The authors acknowledge the financial support provided by the National Key Research and Development Program of China (2022YFB3806300).

Institutional Review Board Statement: Not applicable.

Informed Consent Statement: Not applicable.

Data Availability Statement: The data are contained within this article.

Conflicts of Interest: Authors Haoran Peng and Kang Yuan are employed by the company BGRIMM Advanced Materials Science & Technology Co., Ltd. The remaining authors declare that the research was conducted in the absence of any commercial or financial relationships that could be construed as a potential conflict of interest.

References

1. Lu, X.G.; Yuan, J.Y.; Li, G.; Xu, M.Y.; Lu, G.Q.; Zhang, Y.X.; Yuan, F.H.; Huang, J.Q.; Deng, L.H.; Jiang, J.N.; et al. Plasma-sprayed Yb₃Al₅O₁₂ as a novel thermal barrier coating for gas turbine applications. *J. Eur. Ceram. Soc.* **2024**, *44*, 5138–5153. [[CrossRef](#)]
2. Brindley, W.J.; Miller, R.A. TBCs for better engine efficiency. *Adv. Mater. Process* **1989**, *136*, 29–33.
3. Song, J.B.; Wang, L.S.; Dong, H.; Yao, J.T. Long lifespan thermal barrier coatings overview: Materials, manufacturing, failure mechanisms, and multiscale structural design. *Ceram. Int.* **2023**, *49*, 1–23. [[CrossRef](#)]
4. Krogstad, J.A.; Kramer, S.; Lipkin, D.M.; Johnson, C.A.; Mitchell, D.R.G.; Cairney, J.M.; Levi, C.G. Phase Stability of t'-Zirconia-Based Thermal Barrier Coatings: Mechanistic Insights. *J. Am. Ceram. Soc.* **2011**, *94*, 168–177. [[CrossRef](#)]
5. Rezanka, S.; Mack, D.E.; Mauer, G.; Sebold, D.; Guillon, O.; Vaßen, R. Investigation of the resistance of open-column-structured PS-PVD TBCs to erosive and high-temperature corrosive attack. *Surf. Coat. Technol.* **2017**, *324*, 222–235. [[CrossRef](#)]
6. Hospach, A.; Mauer, G.; Vassen, R.; Stover, D. Columnar-structured thermal barrier coatings (TBCs) by thin film low-pressure spraying (LPPS-TF). *Therm. Spray Technol.* **2011**, *20*, 116–120. [[CrossRef](#)]
7. Bakan, E.; Vaßen, R. Ceramic top coats of plasma-sprayed thermal barrier coatings: Materials, processes, and properties. *J. Therm. Spray Technol.* **2017**, *26*, 992–1010. [[CrossRef](#)]
8. Yang, L.X.; Yang, F.; Long, Y.; Zhao, Y.; Xiong, X.; Zhao, X.F.; Xiao, P. Evolution of residual stress in air plasma sprayed yttria stabilised zirconia thermal barrier coatings after isothermal treatment. *Surf. Coat. Technol.* **2014**, *251*, 98–105. [[CrossRef](#)]
9. Zhao, X.L.; Liu, W.; Li, C.; Yan, G.; Wang, Q.W.; Yang, L.; Zhou, Y.C. Solid Particle Erosion Behavior of La₂Ce₂O₇/YSZ Double-Ceramic-Layer and Traditional YSZ Thermal Barrier Coatings at High Temperature. *Coatings* **2022**, *12*, 1638. [[CrossRef](#)]
10. Chen, D.; Wang, Q.S.; Liu, Y.B.; Ning, X.J. Microstructure, thermal characteristics, and thermal cycling behavior of the ternary rare earth oxides (La₂O₃, Gd₂O₃, and Yb₂O₃) co-doped YSZ coatings. *Surf. Coat. Technol.* **2020**, *403*, 126387. [[CrossRef](#)]
11. Yan, Z.; Peng, H.R.; Yuan, K.; Zhang, X. Optimization of Yb₂O₃-Gd₂O₃-Y₂O₃ Co-Doped ZrO₂ Agglomerated and Calcined Powders for Air Plasma Spraying. *Coatings* **2021**, *11*, 373. [[CrossRef](#)]
12. Guo, S.; Hao, Z.H.; Ma, R.L.; Wang, P.; Shi, L.Y.; Shu, Y.C.; He, J.L. Preparation of spherical WC-Co powder by spray granulation combined with radio frequency induction plasma spheroidization. *Ceram. Int.* **2023**, *49*, 12372–12380. [[CrossRef](#)]
13. Li, G.F.; Wang, D.; Wu, Y.H.; Li, C.; Cheng, C.Y.; Yang, L.; Zhou, Y.C. The solid solution and microstructural evolution of WC doped Hf-Ta-C powders by induction plasma spheroidization. *Powder Technol.* **2023**, *419*, 118338. [[CrossRef](#)]

14. Hossein, M.S.; Jackson, C.; Zane, Y. A review on ICP powder plasma spheroidization process parameters. *Int. J. Refract. Met. Hard Mater.* **2021**, *103*, 105764.
15. Ko, S.; Koo, S.; Cho, W.; Hwnag, K.; Kim, J. Synthesis of SiC nano-powder from organic precursors using RF inductively coupled thermal plasma. *Ceram. Int.* **2012**, *38*, 1959–1963. [[CrossRef](#)]
16. Saifutdinova, A.A.; Saifutdinov, A.I.; Gainullina, S.V.; Timerkaev, B.A. Modeling the parameters of an atmospheric pressure dielectric barrier discharge controlled by the shape of the applied voltage. *IEEE Trans. Plasma Sci.* **2022**, *50*, 1144–1156. [[CrossRef](#)]
17. Christian, B.; Ilya, T.; Jörg, H.; Pierre, B.J. Numerical modeling of an inductively coupled plasma torch using OpenFOAM. *Comput. Fluids* **2021**, *216*, 104807.
18. Shi, T.J.; Bai, B.T.; Peng, H.R.; Yuan, K.; Han, R.F.; Zhou, Q.; Pang, X.X.; Zhang, X.; Yan, Z. Improved thermal shock resistance of GYYZO-YSZ double ceramic layer TBCs induced by induction plasma spheroidization. *Surf. Coat. Technol.* **2024**, *477*, 130372. [[CrossRef](#)]
19. Nagulin, K.; Nazarov, R.; Efimochkin, I.; Gilmutdinov, A. Optimization of radio-frequency plasma parameters for spheroidization of zirconium oxide powders. *Surf. Coat. Technol.* **2020**, *382*, 125196. [[CrossRef](#)]
20. Ye, R.; Ishigaki, T.; Jurewicz, J.; Proulx, P.; Boulos, M.I. In-Flight Spheroidization of Alumina Powders in Ar-H₂ and Ar-N₂ Induction Plasmas. *Plasma Chem. Plasma Process.* **2004**, *24*, 555–571. [[CrossRef](#)]
21. Dire, R.M.; Bissett, H.; Delport, D.; Premalal, K. Evaluation of spheroidized tungsten carbide powder produced by induction plasma melting. *South Afr. Inst. Min. Metall.* **2021**, *121*, 175–179. [[CrossRef](#)]
22. Bissett, H.; Walt, D.V.I.; Havenga, J. Titanium and zirconium metal powder spheroidization by thermal plasma processes. *J. South Afr. Inst. Min. Metall.* **2015**, *115*, 937–942. [[CrossRef](#)]
23. Shin, D.; Gitzhofer, F.; Moreau, C. Influence of induction plasma gas composition on Ti coatings microstructure and composition. In *Thermal Spray 2004: Advances in Technology and Application: Proceedings of the International Thermal Spray Conference, Osaka, Japan, 10–12 May 2004*; ASM International: Tokyo, Japan, 2004; pp. 825–830.
24. Vassen, M.O.R.; Jarligo, T.; Steinke, D.E.; Mack, D. Stoeber, Overview on advanced thermal barrier coatings. *Surf. Coat. Technol.* **2010**, *205*, 938–942. [[CrossRef](#)]
25. Shi, M.C.; Xue, Z.L.; Zhang, Z.Y.; Ji, X.J.; Byon, E.; Zhang, S.H. Effect of spraying powder characteristics on mechanical and thermal shock properties of plasma-sprayed YSZ thermal barrier coating. *Surf. Coat. Technol.* **2020**, *395*, 125913. [[CrossRef](#)]

Disclaimer/Publisher's Note: The statements, opinions and data contained in all publications are solely those of the individual author(s) and contributor(s) and not of MDPI and/or the editor(s). MDPI and/or the editor(s) disclaim responsibility for any injury to people or property resulting from any ideas, methods, instructions or products referred to in the content.